nature geoscience

Article

https://doi.org/10.1038/s41561-023-01327-8

Recurrence time and size of Chilean earthquakes influenced by geological structure

Received: 21 January 2023

Accepted: 19 October 2023

Published online: 15 December 2023

Check for updates

Joaquín Julve[1,2] ✉, Sylvain Barbot[3], Marcos Moreno[4], Andrés Tassara[1,2], Rodolfo Araya[5], Nicole Catalán[1], Jorge G. F. Crempien[4] & Valeria Becerra-Carreño[4]

In 1960, the giant Valdivia earthquake (moment magnitude, M_w, 9.5), the largest earthquake ever recorded, struck the Chilean subduction zone, rupturing the entire depth of the seismogenic zone and extending for 1,000 km along strike. The first sign of new seismic energy release since 1960 occurred in 2017 with the Melinka earthquake (M_w 7.6), which affected only a portion of the deepest part of the seismogenic zone. Despite the recognition that rupture characteristics and rheology vary with depth, the mechanical controls behind such variations of earthquake size remain elusive. Here we build quasi-dynamic simulations of the seismic cycle in southern Chile including frictional and viscoelastic properties, drawing upon a compilation of geological and geophysical insights to explain the recurrence times of recent, historic, and palaeoseismic earthquakes and the distribution of fault slip and crustal deformation associated with the Melinka and Valdivia earthquakes. We find that the frictional and rheological properties of the forearc, which are primarily controlled by the geological structure and fluid distribution at the megathrust, govern the magnitude and recurrence patterns of earthquakes in Chile.

Earth's largest earthquakes, frequently accompanied by devastating tsunamis, are hosted at subduction zones, outlying the key importance to understand subduction dynamics during the seismic cycle. This process is controlled by the structure of the Accretionary Prism and the fabric of the megathrust—the seismogenic interface that separates the downgoing oceanic lithosphere from the upper plate. Earthquakes originate from a frictional instability at the plate interface, primarily affected by the lithology, temperature, and fluid content of the fault zone, leading to a stratification of source properties[1–3]. Numerous studies have shown variability in rupture width and slip of earthquakes in different depth domains, encompassing great ruptures (moment magnitude, M_w, > 8.5) with a trench-breaking feature[4], and large blind ruptures (7 < M_w < 8.5) nucleated within the interseismically locked region as illustrated by palaeoseismic and instrumental record at the Japan[5], Sunda[6] and Aleutian[7] trenches. The succession of large and great ruptures at the subduction megathrust modulates the size and frequency of earthquakes, but the underlying mechanics are uncertain.

The Southern Chile Subduction Zone (SCSZ) produced the M_w 9.5 Valdivia 1960 mega-quake[8], the largest earthquake on record, which was followed 56 years later by the M_w 7.6 Melinka earthquake[9] (Fig. 1). The 2016 Melinka rupture concentrated in the down-dip limit of the Valdivia earthquake, sparing the central part of the seismogenic zone

[1]Departamento Ciencias de la Tierra, Facultad de Ciencias Químicas, University of Concepción, Concepción, Chile. [2]Millennium Nucleus The Seismic Cycle Along Subduction Zones CYCLO, Valdivia, Chile. [3]Department of Earth Sciences, University of Southern California, Los Angeles, CA, USA. [4]Department of Structural and Geotechnical Engineering, Pontifical Catholic University of Chile, Santiago, Chile. [5]Departamento de Ingeniería Matemática, University of Concepción, Concepción, Chile. ✉e-mail: jjulve@udec.cl

https://doi.org/10.1038/s41561-023-01327-8

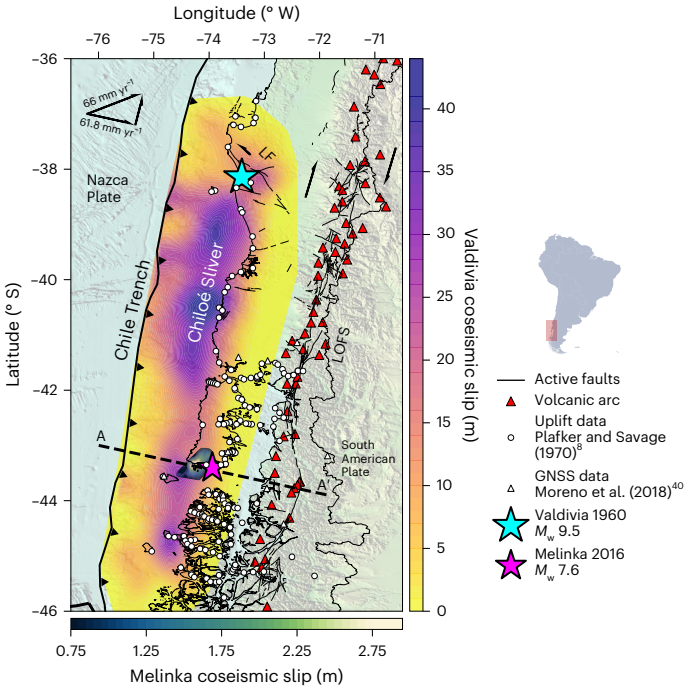

Fig. 1 | Tectonic setting of the SCSZ. Coseismic slip model of the Valdivia earthquake[60] and coseismic slip model of the Melinka earthquake[40]. LOFS, Liquiñe–Ofqui Fault System; LF, Lanalhue Fault and active crustal faults[64]. The Chiloé Sliver[65] is bounded by the trench, the LOFS and the LF. We consider the slip distribution and seismic cycles along the representative cross section A–A′. Basemap from GEBCO[66].

that is currently locked[9]. The sequence of a full-depth rupture followed by seismic resurgence in the deep segment of the seismogenic zone, along with the extensive geodetic, geophysical and palaeoseismological record associated with the 1960 mainshock, is fundamental to explore the factors that control the slip evolution and recurrence of subduction earthquakes.

Here we implement a numerical model of the seismic cycle at the SCSZ with depth-variable rate- and state-dependent frictional properties on the megathrust and thermally activated rheological properties in the subducting oceanic asthenosphere and over-turning mantle wedge underneath the upper plate. We base the constitutive properties on our own thermal model of the SCSZ ('Temperature model' in Methods) and the lithology of the subducted channel and surrounding lithosphere. We construct a cross section of the SCSZ with a structural layout compatible with geological and geophysical observations. We then explore how the recurrence periods, slip and deformation of large and great earthquakes are controlled by the frictional properties of the megathrust. Our optimal model, based on a sensitivity analysis of the main parameters controlling frictional resistance, such as rheology and pore pressure ratio (λ), allows us to match multiple measurements at the earthquake cycle in Chile, providing new insights into the mechanical control of subduction earthquakes.

Modelling the subduction seismic cycle of the southern Andes

Using quasi-dynamic numerical simulations that resolve the mechanical interactions between a frictional megathrust and a temperature-controlled viscoelastic asthenosphere, we simulate the occurrence of great (Valdivia-like) and large (Melinka-like) ruptures throughout the seismic cycle of the SCSZ. The model resolves all phases of the seismic cycle, including nucleation and propagation of earthquakes, along with afterslip and viscoelastic relaxation that follow the mainshocks. We build a model of subduction dynamics along a representative cross section (Fig. 2a) assuming a 61.8 mm per year convergence rate between the Nazca and South American plates in the trench-perpendicular direction[10]. The structural layout is constrained by the Slab2 model[11], seismicity[12,13], seismic wave tomography and reflection profiles[14–18], and gravity-constrained density models[16,19]. The outer wedge is defined by the highly deformed Accretionary Prism[14]. The inner wedge extends from the outer arc high to the continental slope, featuring inactive accretion structures. The Lower Seismogenic Zone encompasses the palaeoprism up to the intersection with the Moho, presenting underplating structures[17,20] and seismic wave velocities[14] and density[16] anomalies suggesting the presence of a high ratio of compressional to shear wave velocities (V_p/V_s)[21] and a static backstop. Eastwards, the continental crust transitions from Permo–Triassic metamorphosed units to granitoids of the North Patagonian Batholith[22]. The Liquiñe–Ofqui Fault System[23] (LOFS) deforms the granitoids and bounds the eastern part of the Chiloé Sliver (Fig. 1a). Beneath the continental crust, the megathrust underlies the Metamorphic Belt and the Serpentinized Mantle Wedge, terminating at the 650 °C isotherm at about 85 km depth. From there, the downgoing slab is permanently coupled to the mantle wedge that deforms by viscous flow.

We assume that the frictional behaviour of the megathrust is controlled by a slip-rate- and state-dependent friction law[5,24] (equation (3) in Methods):

$$\tau = \mu_0 \bar{\sigma} \left(\frac{V}{V_0}\right)^{\frac{a}{\mu_0}} \left(\frac{\theta V_0}{L}\right)^{\frac{b}{\mu_0}}$$

where μ_0 is the effective coefficient of friction, $\bar{\sigma}$ is the effective normal stress, V and V_0 are the instantaneous and reference velocities at the fault interface, θ is a state variable that follows an evolution law allowing healing at stationary contacts[5] and L is a characteristic slip distance. The direct and steady-state velocity dependence of friction is controlled by the parameters a and $a-b$, respectively, with $a-b<0$ corresponding to velocity-weakening, potentially unstable friction and $a-b>0$ giving rise to velocity-strengthening friction, which inhibits rupture nucleation and propagation. Guided by the expected mineralogical composition at the plate interface and considering the thermal structure, we use laboratory-derived information extracted from fault gouges to constrain the frictional parameters assigned to the megathrust (Table 1). The depth-dependent thermal and compositional stratification leads to a structural model for the fault with five down-dip segments with distinct properties (Fig. 2b).

Seismic wave profiles[14] and sedimentary fluxes[25] indicate a trench fill varying from 1 to 3 km (ref. 20), reflecting the strong denudation of the exhumed North Patagonian Batholith[26] during the last Pliocene glaciation[27]. The erosion of the Andean Cordillera[28] allows us to assume that friction in the outer wedge is controlled by a mixed phyllosilicates and quartz composition. We use average values from laboratory results on fault gouges composed of about 50% quartz and 50% clay minerals at low temperatures[29,30], yielding $a-b=2\times10^{-3}$. As ~80% of the sediments enter the subduction channel[31], we assume that the seismogenic zone is controlled by a granitic composition[32], rather than by altered basalts from the subducting slab (Fig. 2a), leading to $a-b=-1\times10^{-2}$ in the Upper and Lower Seismogenic Zone (Fig. 2b). Finally, background seismicity and locking degree models show the transition from a locked to creeping fault at 35 km depth[12,33], suggesting that the megathrust shifts to velocity-strengthening properties beyond the continental Moho. Fluid-driven serpentinization occurs in the cold mantle wedge, developing a serpentinization front at the plate interface[34]. We assume frictional parameters of serpentinites[35–37] to characterize the two deepest segments. This accounts for the transition from lizardite to antigorite at ~350 °C (ref. 38), leading to $a-b=1.5\times10^{-2}$ underneath the

https://doi.org/10.1038/s41561-023-01327-8

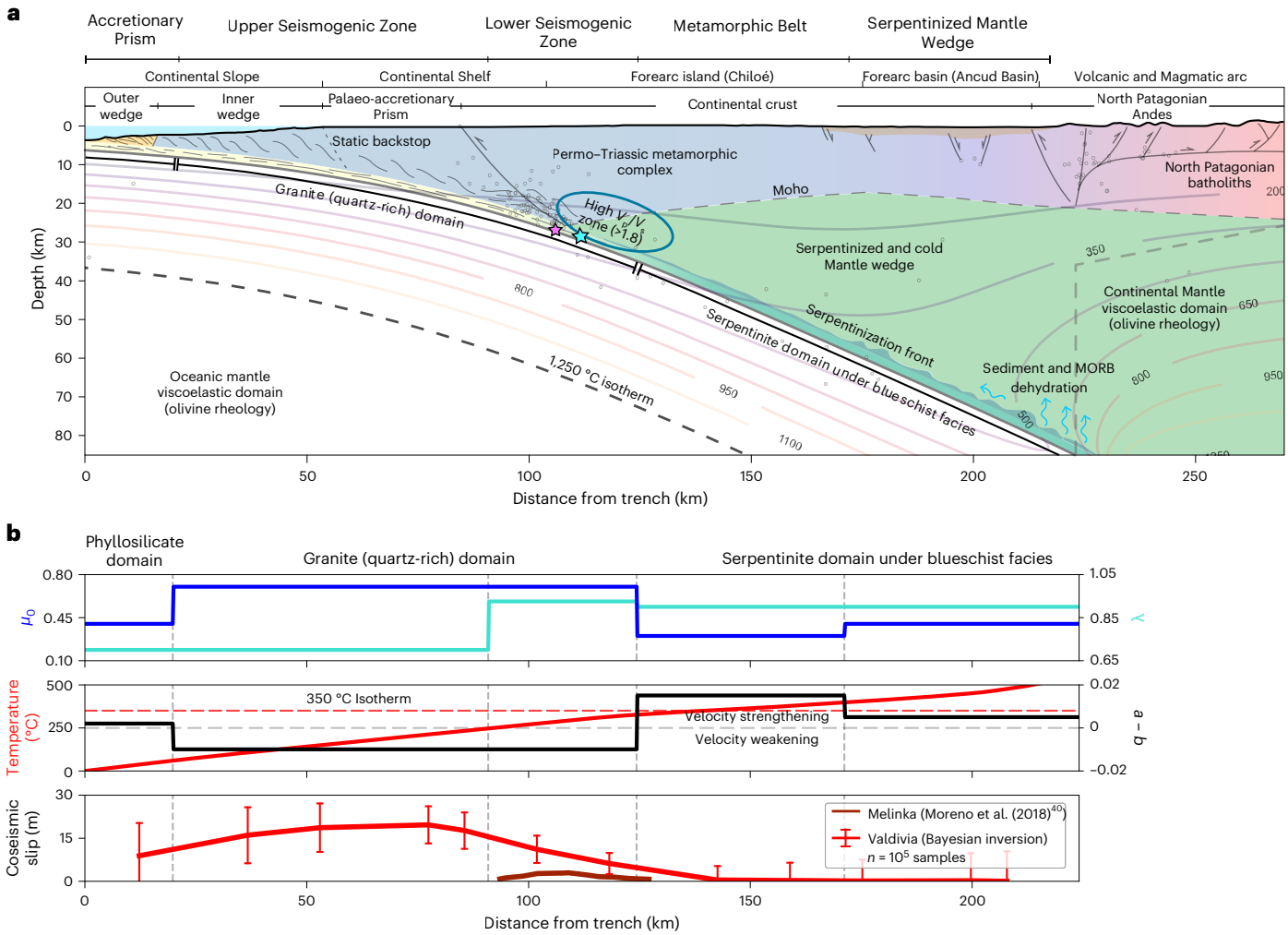

Fig. 2 | Summary of data acquired and set-up of the model. a, Cross section of the SCSZ with the compilation of available data. Crustal faults are from ref. 64, interseismic seismicity is from ref. 12, and outer and inner wedge structures are from ref. 13. Horizontal lines and names at the top of the figure define the down-dip megathrust segments presented in our work. **b**, Set-up of the quasi-dynamic model, μ_0 is the reference coefficient of friction, λ is the pore pressure ratio assumed at each segment, and $a-b$ is the parameter obtained from equation (3) (Methods). The temperature is obtained from our thermal model (Methods) at the plate interface. The Melinka slip was obtained from ref. 9 while the Valdivia slip is the result of our new inversion (Methods), where error bars are one standard deviation.

Table 1 | Frictional parameters of the preferred and initial models

Segment	Mineralogy	References	$a\times10^{-2}$	$b\times10^{-2}$	L (cm)	$a-b\times10^{-2}$	σ (MPa)	σ (MPa) initial	μ	W (km)	λ	λ initial
AP	Phyllosilicates + quartz	29,30	1	0.8	7.5	0.2	45	45	0.4	20	0.7[a]	
LSZ	Granite	32	0.3	1.3	1.5	−1	113	19	0.6	73	0.7	0.95
USZ	Granite	32	0.3	1.3	1	−1	56	15	0.6	30	0.92	0.98
MB	Lizardite	35–37	2	0.5	5	1.5	130	65	0.3	85	0.9	0.9
SMW	Antigorite	35–37	1	0.5	5	0.5	220	110	0.4	102	0.9	0.9

[a]Pore pressure ratio from ref. 39. W is the length of each segment. AP, Accretionary Prism; LSZ, Lower Seismogenic Zone; USZ, Upper Seismogenic Zone; MB, Metamorphic Belt; SMW, Serpentinized Mantle Wedge. The pore pressure ratio at the USZ and LSZ are calibrated based on the recurrence time of large and great palaeoearthquakes and the slip distribution of Melinka-like and Valdivia-like earthquakes (Extended Data Fig. 3) starting from previous estimates[40].

Metamorphic Belt and $a-b=5\times10^{-3}$ below the Serpentinized Mantle Wedge (Fig. 2b).

The effective normal stress on the megathrust depends on the local value of the partial fluid pressure ratio (λ) via $\bar{\sigma}=\sigma_n(1-\lambda)$, where σ_n is the local normal stress based on gravity (equation (14) in 'Pressure and temperature path' in Methods). Our initial set-up considers published estimates of λ at the Accretionary Prism[39] that suggest an overpressure region at the bottom of the seismogenic zone[3,40] (Table 1). To obtain the pressure–temperature path along the fault (Extended Data Fig. 1b), we build a finite-element thermal model based on near-lithostatic pore fluid pressure at megathrust depth[41], where the temperature satisfies the steady-state heat advection–diffusion

equation ('Temperature model' in Methods). The resulting temperature distribution (Extended Data Fig. 1a and Fig. 2a) shows the same depth of the 650 °C isotherm (~85 km) as previous models[42,43] but features a deeper 350 °C isotherm.

For the viscoelastic domain, we assume the rheological parameters of olivine aggregates for transient and steady-state dislocation creep[44,45] and divide the mantle wedge into a serpentinized wet region below the arc and a dry region farther east, establishing a cold-nose configuration[46] (Extended Data Fig. 1a and Extended Data Table 1). Viscoelastic deformation on each volume element is captured by a Burger's assembly of springs and dashpots[45] whereby the anelastic strain rates in the Maxwell and Kelvin elements follow a power-law rheology (equation (7) in 'Fault friction and mantle viscosity' in Methods), which is activated with the background temperature distribution of the finite-element thermal model (equation (13) in 'Temperature model' in Methods).

Finally, we conduct simulations spanning 10,000 years of seismic activity following the distribution of parameters constrained by the geological structure, providing the surface displacement associated with various sequences of total and partial ruptures in the SCSZ (Fig. 3a) and the distribution of down-dip slip. The simulations employ adaptive time steps to capture the details of rupture initiation and propagation and the more quiescent periods in between. To mitigate bias from initial conditions[47], we focus on the last 7,500 years of each simulation during which the patterns of the rupture sequences are stable over time.

Earthquake cycle observations

Decadal records of crustal deformation allow the characterization of the earthquake cycle, in which vertical tectonic displacements modulate the local relative sea level by several metres, while horizontal deformation evolves on a continental scale[48]. The surface deformation associated with the Valdivia earthquake is constrained by an extensive array of biological and anthropogenic markers that capture coseismic and postseismic vertical displacements[8], involving slip on the megathrust but also an eight-year-long viscoelastic flow in the surrounding lithosphere[49]. Coseismic deformation of the Melinka earthquake was registered with Global Navigation Satellite System (GNSS) data[40] and intertidal biotic indicators[50] that describe up to 0.3 m of uplift at the Lower Seismogenic Zone. The occurrence of palaeoseismic trench-breaking ruptures followed by large earthquakes in the following years has also been recorded in sediments at lake and fjords of the SCSZ. The recurrence time for earthquakes with $M_w \geq 8.6$ is 292 ± 93 years (refs. 51,52), while events with $7.7 \leq M_w \leq 8.5$ happen every 139 ± 69 years (ref. 52).

To calibrate the model, we compare our predictions with the estimations of recurrence times for large and great events at the SCSZ[51,52] and with surface deformation of the Melinka[40] and Valdivia[8] earthquakes (Extended Data Fig. 2). We compute the root mean square error between the model results and the available dataset (Extended Data Fig. 3). Using the distribution of pore fluid pressure ratio from the initial model (Table 1), we cannot simultaneously reproduce the recurrence time and the surface deformation after large and great ruptures. We evaluate different configurations of pore fluid pressure ratio at each frictional segment (Extended Data Table 2) while keeping the rest of the frictional parameters constant. The pore fluid pressure ratio distribution that minimizes the root mean square error features $\lambda \geq 0.9$ in the Lower Seismogenic Zone, $0.7 \leq \lambda \leq 0.75$ in the Upper Seismogenic Zone and $\lambda = 0.9$ in the Creeping Zone. We use this configuration hereafter as our preferred model (Table 1) to describe the rupture mechanics and consequent deformation at the SCSZ.

Mechanics and surface deformation of simulated earthquakes

We analyse the seismic cycle at the SCSZ viewing a representative example of fault dynamics of our preferred model between 6,000 to 7,000 years (Fig. 3a). Seismicity predominantly nucleates at the transition from the keel of the continental crust to the cold nose of the mantle wedge corner. Large earthquakes involve partial ruptures (Fig. 3a), which include Melinka-like events (Fig. 3b) that nucleate at the Lower Seismogenic Zone but stopped on their way to the trench. Great ruptures encompass the entire seismogenic zone and the outer wedge (Fig. 3c), with Valdivia-like events (Fig. 3c) showing similar rupture style[53,54] and trench-breaking propagation[55] to the 1960 mega-quake. Despite the assumed velocity-strengthening friction in the outer wedge, all great ruptures break the trench, in line with $M_w > 8.5$ palaeoseismic data[51,56], and uplift models derived from tsunami data after the Valdivia earthquake, indicating up to 4 m of seafloor uplift[55]. Both earthquake types propagate through creep zones resulting from stress concentration at previous event tips (Fig. 3b,c), indicating a mechanical link between large and great earthquakes. This interaction allows the trench to experience coseismic slip during great ruptures and creeping during interseismic periods (Fig. 3b–d).

The preferred model predicts recurrences for large (82 ± 43.4 year) and great (271 ± 70 year) ruptures matching the estimates from palaeoturbidites and tsunami deposits[51,52,57] within uncertainties (Fig. 3e,f). For large earthquakes, the mean recurrence time of simulated events approaches the median recurrence of past earthquakes with $7.7 \leq M_w \leq 8.5$ derived from the geological record and the 56-year lag between the 1960 and 2017 earthquakes. In the simulations, the recurrence times and the coseismic slip of each rupture depend mostly on $\bar{\sigma}$, $a - b$ and the width of the seismogenic zone. There is a trade-off between fitting large recurrence times and data-constrained maximum slip, but our model with the optimized pore fluid pressure generates results within the 95% confidence interval of estimations derived from palaeoseismicity (Extended Data Fig. 3 and Fig. 3e,f).

We compare simulated surface deformation for great and large ruptures with available uplift data eight years after the Valdivia earthquake and coseismic GNSS data following the Melinka earthquake (Extended Data Fig. 2). For each great earthquake, we extract vertical displacement produced by coseismic rupture and eight years of postseismic deformation to obtain a surface vertical profile. The median pattern mirrors the observed eight-year Valdivia earthquake deformation, featuring from west to east offshore uplift, coastal subsidence, and volcanic arc uplift (Fig. 4). Postseismic deformation results from afterslip in the Lower Seismogenic Zone and behind the Metamorphic Belt and viscoelastic uplift in the Accretionary Prism and volcanic arc (Fig. 4). Uplift at the volcanic arc is attributed to the rheological contrast between the cold nose and a high-temperature mantle beneath it, consistent with prior works[49]. Viscoelastic flow in the oceanic asthenosphere causes postseismic uplift near the trench[58]. The magnitude of uplift is not fully compensated by interseismic subsidence in the years after the main event (Extended Data Figs. 4 and 5), explaining the similar magnitude of coseismic and postseismic uplift (Fig. 4a).

The slip distribution of the simulated great ruptures eight years after each mainshock is consistent with a Bayesian estimate of coseismic slip for the Valdivia earthquake[59] (equation (15) in 'Coseismic slip model' in Methods) that is inverted form the same land-level changes data captured eight years after the main event. Our kinematic inversion shows up to 7 m of coseismic slip near the trench (Fig. 4b), like previous results from estimations incorporating tsunami data[55], and has the same maximum slip (around 20 m) as past models that include changes in slab geometry[60]. The minimum uncertainty is observed between 75 to 150 km from the trench, solving the slip distribution at the end of the rupture and thus coinciding with the end of the seismogenic zone at 35 km depth (Figs. 2b and 4b). A small proportion of simulated giant ruptures generate a slightly lower coseismic slip in the seismogenic zone compared with the geodetic model. However, all simulated events and their median profile (black bold line at Fig. 4b) match the slip distribution within uncertainties. All simulated great earthquakes

https://doi.org/10.1038/s41561-023-01327-8

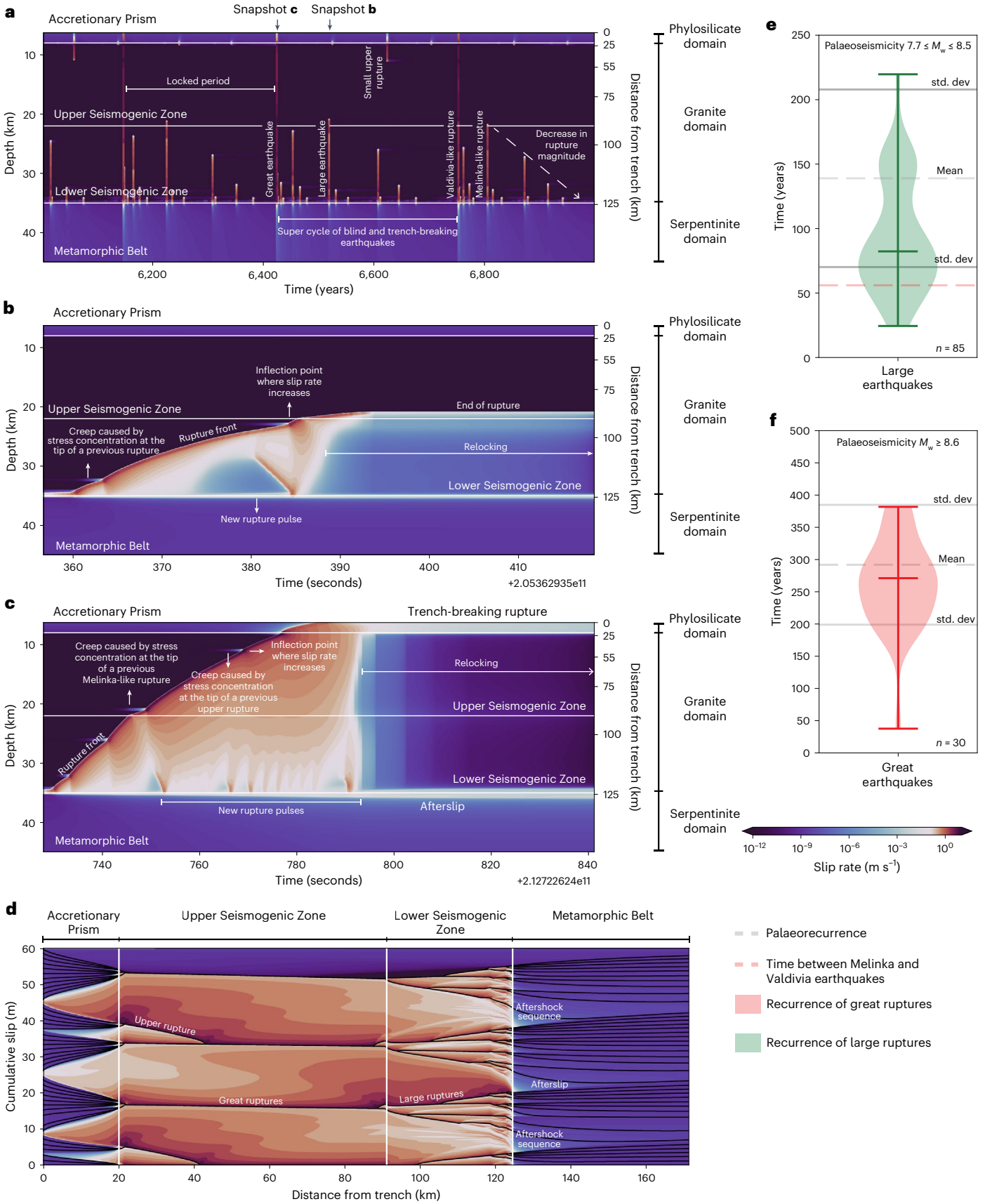

Fig. 3 | Fault dynamics and recurrence times at the SCSZ. a, Slip rate over time of the simulation along the megathrust. **b**, Snapshot of Melinka-like earthquakes at **a**. **c**, Snapshot of Valdivia-like earthquakes at **a**. **d**, The cumulative slip over the same period as **a**; black lines represent the cumulative slip curve every 25 years at the interseismic period. **e**,**f**, Violin plots of recurrence times of simulated events showing median, minimum and maximum values against recurrence times of palaeoseismicity presented as mean values with one standard deviation[51,52,57].

https://doi.org/10.1038/s41561-023-01327-8

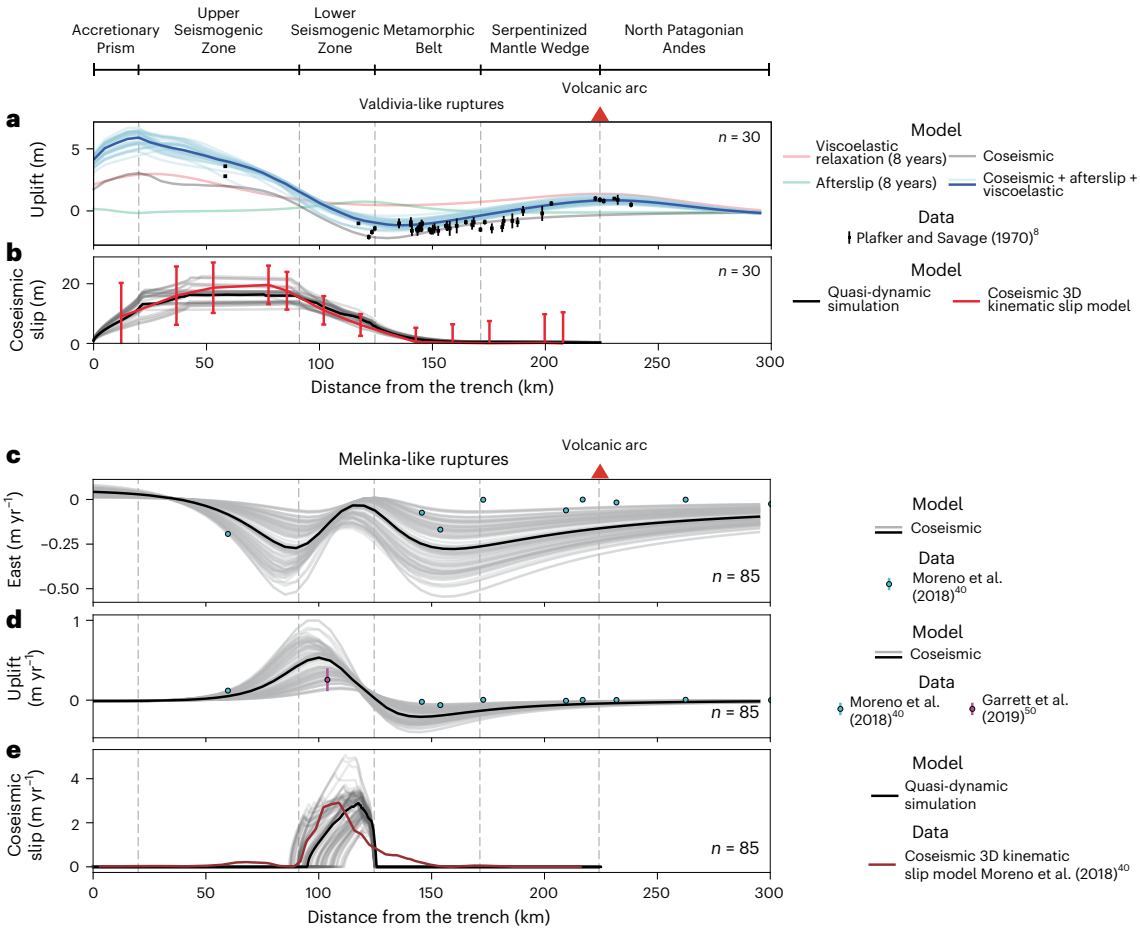

Fig. 4 | Upper crust deformation. a, Comparison between Valdivia-like ruptures with the land-level changes data eight years after the Valdivia earthquake[8] and error bars with mean standard error. Bold lines are the mean curve of each component obtained from all simulated events. **b**, Coseismic slip generated by Valdivia-like ruptures compared against our coseismic slip model (red lines) with one standard deviation (red bars). **c**, Comparison between Melinka-like ruptures and the East component of the GNSS data from the Melinka earthquake[40]. **d**, Comparison between Melinka-like ruptures and the vertical component of the GNSS data from the Melinka earthquake[40] and uplift from intertidal biotic indicators[50] plus two standard deviations (error bars). **e**, Coseismic slip generated by simulated Melinka-like ruptures compared against the model of ref. 40.

generate coseismic slip up to the trench, consistent with the proposed trench-breaking feature of the Valdivia event[55].

Finally, we assess crustal deformation linked to large ruptures by comparing model predictions with data from continuous GNSS displacements[40] and land-level changes[50] following the 2016 Melinka earthquake. Our simulated Melinka-like ruptures (Fig. 4c,d) show a median curve exceeding the immediate coseismic pattern[40]. However, simulations with smaller surface deformation match both horizontal and vertical components of observed data, reproducing coseismic uplift above the Lower Seismogenic Zone inferred from intertidal biotic indicators[50]. The amplitude of median simulated coseismic slip agrees with published models[9,40] but shifts slightly towards the down-dip limit of the seismogenic zone. Large ruptures represent a family of moderate events, inducing surface deformation ranging from tens to hundreds of centimetres, with up to 4 m of coseismic slip concentrated mainly within the Lower Seismogenic Zone (Figs. 3a and 4c–e). Minor disparities between our two-dimensional models and GNSS data of the horizontal component for the Melinka earthquake (Fig. 4c) arise due to source–receiver distance decay variations, particularly noticeable in smaller ruptures. Along-strike rupture propagation is an important aspect of megathrust dynamics[61]. In nature, we expect other Melinka-like earthquakes to initiate at similar depths at different latitudes along the trench axis, but this is not captured within our two-dimensional approximation.

Subduction cycle at the Valdivia segment

Our synoptic model (Fig. 5) integrates down-dip variations in the composition of rocks at the subduction channel, lithospheric temperature distribution and mantle rheology to explain the sequence and recurrence of great and large earthquakes and associated crustal deformation in the SCSZ. Our models underscore the role of geological structure and pore fluid pressure in controlling frictional behaviour governing large and great earthquake sequences (Extended Data Figs. 3 and 4). If no increase in pore fluid pressure is considered, then the time between each kind of earthquake will not match the observations and the amplitude of uplift and subsidence will not reproduce the coseismic and postseismic data after the Valdivia earthquake. Our models do not explain the origin of fluid concentration at the Lower Seismogenic Zone, but our pressure–temperature path (Extended Data Fig. 1b) is consistent with in situ fluid release from prograde metamorphism of metapelites[62,63] at the observed high V_p/V_s ratio zone[21], outlying the effect of dehydration processes on earthquake mechanics.

Mineralogy at the plate interface also plays an important role. Neglecting sediment input from the erosion of the continental crust, and thus allowing altered oceanic plate basalt to govern friction at the megathrust, fails to explain the eight-year deformation curve following great earthquakes (Extended Data Fig. 4a). Enlarging the seismogenic zone width displaces the pattern of surface deformation and coseismic slip inland compared to observations, suggesting that the bottom of

https://doi.org/10.1038/s41561-023-01327-8

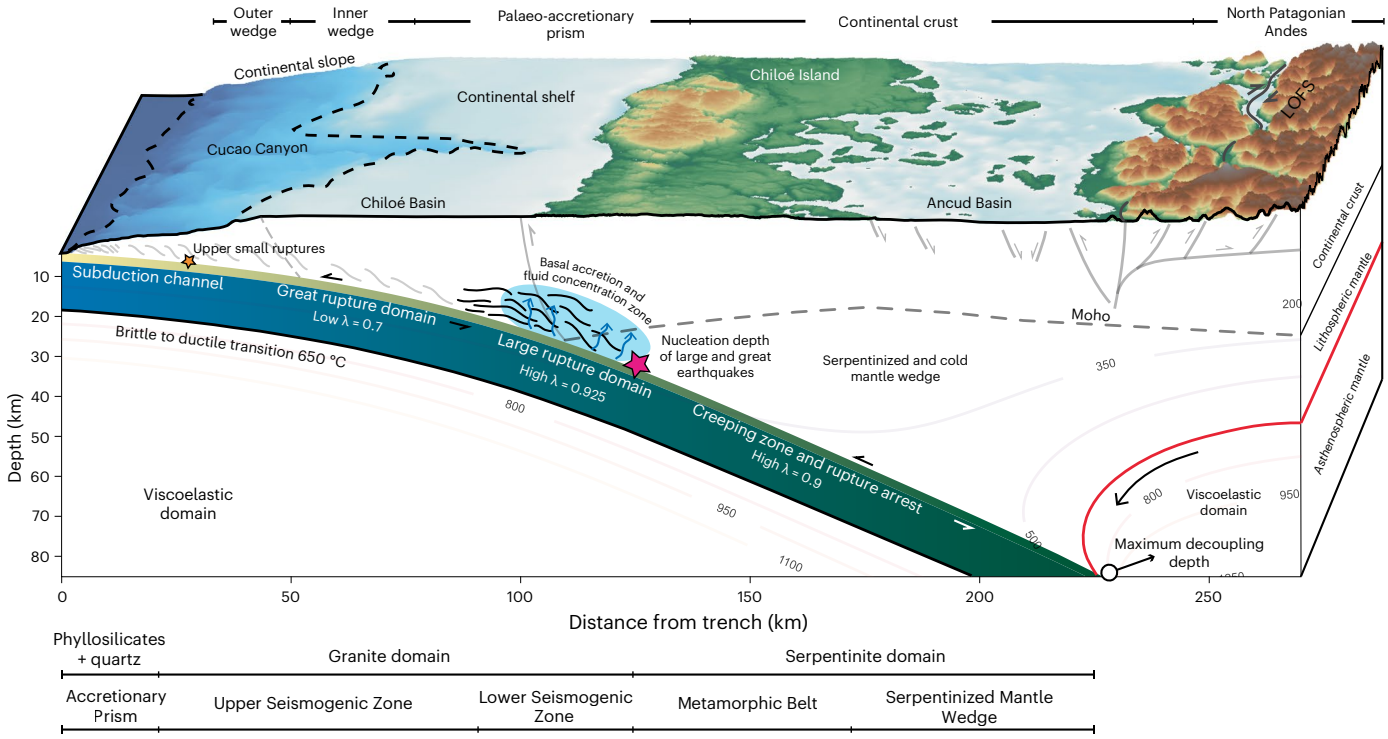

Fig. 5 | Conceptual model of the SCSZ integrating insights from quasi-dynamic simulation and compiled data. λ values are the ones calibrated to our preferred model. Nucleation depth is referred to the depth at which large and great ruptures start. Water concentration region is inferred from in situ fluid release[62]. Basal accretion structures are interpreted from seismic wave profiles[17,20]. Isotherms are obtained from our modelled thermal distribution. Basemap from ref. 67, NASA.

the seismogenic zone may be influenced by fluids and/or the continental Moho (Fig. 5), rather than exclusively by megathrust temperature distribution (Extended Data Fig. 4b,c).

Numerical models constrained by geological and geophysical data, such as presented here, provide an ideal medium to integrate and test geodynamics processes throughout the seismic cycle of megathrust earthquakes, with possible applications at other subduction zones worldwide. Given the spatial relationship between fluid concentration depth and forearc structure at the SCSZ (Fig. 5), we propose that the seismic cycle depends on the thermodynamic conditions at the plate interface associated with the resulting depth-dependent lithology, hydrothermal regime and geological structure, leading to a fluid–rock interaction along the seismogenic megathrust that impacts the stability of frictional sliding.

Online content

Any methods, additional references, Nature Portfolio reporting summaries, source data, extended data, supplementary information, acknowledgements, peer review information; details of author contributions and competing interests; and statements of data and code availability are available at https://doi.org/10.1038/s41561-023-01327-8.

References

1. Lay, T. et al. Depth-varying rupture properties of subduction zone megathrust faults. *J. Geophys. Res. Solid Earth* **117**, B04311 (2012).
2. Scholz, C. H. Earthquakes and friction laws. *Nature* **391**, 37–42 (1998).
3. Saffer, D. M. & Tobin, H. J. Hydrogeology and mechanics of subduction zone forearcs: fluid flow and pore pressure. *Annu Rev. Earth Planet Sci.* **39**, 157–186 (2011).
4. Qiu, Q. & Barbot, S. Tsunami excitation in the outer wedge of global subduction zones. *Earth Sci. Rev.* **230**, 104054 (2022).
5. Barbot, S. Frictional and structural controls of seismic super-cycles at the Japan trench. *Earth Planets Space* **72**, 63 (2020).
6. Lay, T. The surge of great earthquakes from 2004 to 2014. *Earth Planet. Sci. Lett.* **409**, 133–146 (2015).
7. Ye, L., Lay, T., Kanamori, H., Yamazaki, Y. & Cheung, K. F. The 22 July 2020 M_w 7.8 Shumagin seismic gap earthquake: partial rupture of a weakly coupled megathrust. *Earth Planet. Sci. Lett.* **562**, 116879 (2021).
8. Plafker, G. & Savage, J. C. Mechanism of the Chilean earthquakes of May 21 and 22, 1960. *Geol. Soc. Am. Bull.* **81**, 1001–1030 (1970).
9. Ruiz, S. et al. Reawakening of large earthquakes in south central Chile: the 2016 M_w 7.6 Chiloé event. *Geophys. Res. Lett.* **44**, 6633–6640 (2017).
10. Quiero, F., Tassara, A., Iaffaldano, G. & Rabbia, O. Growth of Neogene Andes linked to changes in plate convergence using high-resolution kinematic models. *Nat. Commun.* **13**, 1339 (2022).
11. Hayes, G. P. et al. Slab2, a comprehensive subduction zone geometry model. *Science* **362**, 58–61 (2018).
12. Lange, D. et al. Seismicity and geometry of the South Chilean subduction zone (41.5° S–43.5° S): implications for controlling parameters. *Geophys. Res. Lett.* **34**, L06311 (2007).
13. Bohm, M. et al. The southern Andes between 36° and 40° S latitude: seismicity and average seismic velocities. *Tectonophysics* **356**, 275–289 (2002).
14. Contreras-Reyes, E., Flueh, E. R. & Grevemeyer, I. Tectonic control on sediment accretion and subduction off south central Chile: implications for coseismic rupture processes of the 1960 and 2010 megathrust earthquakes. *Tectonics* **29**, TC6018 (2010).
15. Bangs, N. L. et al. Basal accretion along the South Central Chilean margin and its relationship to great earthquakes. *J. Geophys. Res. Solid Earth* **125**, e2020JB019861 (2020).

16. Maksymowicz, A., Montecinos-Cuadros, D., Díaz, D., Segovia, M. J. & Reyes, T. Forearc density structure of the overriding plate in the northern area of the giant 1960 Valdivia earthquake. *Solid Earth* **13**, 117–136 (2022).
17. Maksymowicz, A. et al. Deep structure of the continental plate in the South-Central Chilean margin: metamorphic wedge and implications for megathrust earthquakes. *J. Geophys. Res. Solid Earth* **126**, e2021JB021879 (2021).
18. Scherwath, M. et al. Deep lithospheric structures along the southern central Chile margin from wide-angle *P*-wave modelling. *Geophys. J. Int.* **179**, 579–600 (2009).
19. Tassara, A. & Echaurren, A. Anatomy of the Andean subduction zone: three-dimensional density model upgraded and compared against global-scale models. *Geophys. J. Int.* **189**, 161–168 (2012).
20. Krawczyk, C. M. et al. in *The Andes* (eds Oncken, O. et al.) 171–192 (Springer, 2006); https://doi.org/10.1007/978-3-540-48684-8_8
21. Dzierma, Y. et al. Seismic velocity structure of the slab and continental plate in the region of the 1960 Valdivia (Chile) slip maximum—insights into fluid release and plate coupling. *Earth Planet. Sci. Lett.* https://doi.org/10.1016/j.epsl.2012.02.006 (2012).
22. Echaurren, A. et al. Fore-to-retroarc crustal structure of the North Patagonian margin: how is shortening distributed in Andean-type orogens?. *Glob. Planet. Change* **209**, 103734 (2022).
23. Cembrano, J., Hervé, F. & Lavenu, A. The Liquiñe Ofqui fault zone: a long-lived intra-arc fault system in southern Chile. *Tectonophysics* **259**, 55–66 (1996).
24. Barbot, S. Slow-slip, slow earthquakes, period-two cycles, full and partial ruptures, and deterministic chaos in a single asperity fault. *Tectonophysics* **768**, 228171 (2019).
25. Kukowski, N. & Oncken, O. in *The Andes* (eds Oncken, O. et al.) 217–236 (Springer, 2006); https://doi.org/10.1007/978-3-540-48684-8_10
26. Genge, M. C. et al. The role of slab geometry in the exhumation of Cordilleran-type orogens and their forelands: insights from northern Patagonia. *Geol. Soc. Am. Bull.* **133**, 2535–2548 (2021).
27. Melnick, D. & Echtler, H. P. Inversion of forearc basins in south-central Chile caused by rapid glacial age trench fill. *Geology* **34**, 709–712 (2006).
28. Adriasola, A. C., Thomson, S. N., Brix, M. R., Hervé, F. & Stöckhert, B. Postmagmatic cooling and late Cenozoic denudation of the North Patagonian Batholith in the Los Lagos region of Chile, 41°–42°15′S. *Int. J. Earth Sci.* **95**, 504–528 (2006).
29. Tembe, S., Lockner, D. A. & Wong, T.-F. Effect of clay content and mineralogy on frictional sliding behavior of simulated gouges: Binary and ternary mixtures of quartz, illite, and montmorillonite. *J. Geophys. Res. Solid Earth* https://doi.org/10.1029/2009jb006383 (2010).
30. den Hartog, S. A. M., Niemeijer, A. R. & Spiers, C. J. New constraints on megathrust slip stability under subduction zone P–T conditions. *Earth Planet. Sci. Lett.* https://doi.org/10.1016/j.epsl.2012.08.022353, 240-252 (2012).
31. Behrmann, J. H. & Kopf, A. Balance of tectonically accreted and subducted sediment at the Chile triple junction. *Int. J. Earth Sci.* **90**, 753–768 (2001).
32. Liu, Y. & Rice, J. R. Slow slip predictions based on granite and gabbro friction data compared to GPS measurements in northern Cascadia. *J. Geophys. Res. Solid Earth* https://doi.org/10.1029/2008jb006142 (2009).
33. Melnick, D. et al. Back to full interseismic plate locking decades after the giant 1960 Chile earthquake. *Nat. Commun.* **9**, 3527 (2018).
34. Angiboust, S., Wolf, S., Burov, E., Agard, P. & Yamato, P. Effect of fluid circulation on subduction interface tectonic processes: insights from thermo-mechanical numerical modelling. *Earth Planet. Sci. Lett.* **357–358**, 238–248 (2012).
35. Okazaki, K. & Katayama, I. Slow stick slip of antigorite serpentinite under hydrothermal conditions as a possible mechanism for slow earthquakes. *Geophys. Res. Lett.* **42**, 1099–1104 (2015).
36. Takahashi, M. et al. On the transient response of serpentine (antigorite) gouge to stepwise changes in slip velocity under high-temperature conditions. *J. Geophys. Res. Solid Earth* https://doi.org/10.1029/2010jb008062 (2011).
37. Moore, D. E. & Lockner, D. A. Frictional strengths of talc-serpentine and talc-quartz mixtures. *J. Geophys. Res. Solid Earth* https://doi.org/10.1029/2010jb007881 (2011).
38. Schwartz, S. et al. Pressure–temperature estimates of the lizardite/antigorite transition in high pressure serpentinites. *Lithos* https://doi.org/10.1016/j.lithos.2012.11.023 (2013).
39. Saffer, D. M. & Wallace, L. M. The frictional, hydrologic, metamorphic and thermal habitat of shallow slow earthquakes. *Nat. Geosci.* **8**, 594–600 (2015).
40. Moreno, M. et al. Chilean megathrust earthquake recurrence linked to frictional contrast at depth. *Nat. Geosci.* **11**, 285–290 (2018).
41. Araya, R., Cárcamo, C. & Poza, A. H. A stabilized finite element method for the Stokes–Temperature coupled problem. *Appl. Numer. Math.* **187**, 24–49 (2023).
42. Spinelli, G. A., Wada, I., He, J. & Perry, M. The thermal effect of fluid circulation in the subducting crust on slab melting in the Chile subduction zone. *Earth Planet. Sci. Lett.* **434**, 101–111 (2016).
43. Völker, D., Grevemeyer, I., Stipp, M., Wang, K. & He, J. Thermal control of the seismogenic zone of southern central Chile. *J. Geophys. Res. Solid Earth* **116**, B10305 (2011).
44. Karato, S.-I. & Jung, H. Effects of pressure on high-temperature dislocation creep in olivine. *Philos. Mag.* https://doi.org/10.1080/01418610210000025829 (2010).
45. Masuti, S., Barbot, S. D., Karato, S.-I., Feng, L. & Banerjee, P. Upper-mantle water stratification inferred from observations of the 2012 Indian Ocean earthquake. *Nature* **538**, 373–377 (2016).
46. Wada, I., Rychert, C. A. & Wang, K. Sharp thermal transition in the forearc mantle wedge as a consequence of nonlinear mantle wedge flow. *Geophys. Res. Lett.* **38**, L13308 (2011).
47. Erickson, B. A. et al. The community code verification exercise for Simulating Sequences of Earthquakes and Aseismic Slip (SEAS). *Seismol. Res. Lett.* **91**, 874–890 (2020).
48. Weiss, J. R. et al. Illuminating subduction zone rheological properties in the wake of a giant earthquake. *Sci. Adv.* **5**, eaax6720 (2019).
49. Luo, H. & Wang, K. Postseismic geodetic signature of cold forearc mantle in subduction zones. *Nat. Geosci.* **14**, 104–109 (2021).
50. Garrett, E., Brader, M., Melnick, D., Bedford, J. & Aedo, D. First field evidence of coseismic land-level change associated with the 25 December 2016 M_w7.6 Chiloé, Chile, earthquake. *Bull. Seismol. Soc. Am.* **109**, 87–98 (2019).
51. Wils, K. et al. Seismo-turbidites in Aysén Fjord (southern Chile) reveal a complex pattern of rupture modes along the 1960 megathrust earthquake segment. *J. Geophys. Res. Solid Earth* **125**, e2020JB019405 (2020).
52. Moernaut, J. et al. Larger earthquakes recur more periodically: new insights in the megathrust earthquake cycle from lacustrine turbidite records in South-Central Chile. *Earth Planet. Sci. Lett.* **481**, 9–19 (2018).
53. Cifuentes, I. L. The 1960 Chilean earthquakes. *J. Geophys. Res. Solid Earth* **94**, 665–680 (1989).
54. Krawczyk, C. Amphibious seismic survey images plate interface at 1960 Chile Earthquake. *Eos Trans. Am. Geophys. Union* **84**, 301–305 (2003).

55. Ho, T.-C., Satake, K., Watada, S. & Fujii, Y. Source estimate for the 1960 Chile earthquake from joint inversion of geodetic and transoceanic tsunami data. *J. Geophys. Res. Solid Earth* **124**, 2812–2828 (2019).
56. Hocking, E. P., Garrett, E., Aedo, D., Carvajal, M. & Melnick, D. Geological evidence of an unreported historical Chilean tsunami reveals more frequent inundation. *Commun. Earth Environ.* **2**, 245 (2021).
57. Kempf, P., Moernaut, J. & De Batist, M. Bimodal recurrence pattern of tsunamis in south-central Chile: a statistical exploration of paleotsunami data. *Seismol. Res. Lett.* **90**, 194–202 (2019).
58. Luo, H. & Wang, K. Finding simplicity in the complexity of postseismic coastal uplift and subsidence following great subduction earthquakes. *J. Geophys. Res. Solid Earth* https://doi.org/10.1029/2022jb024471 (2022).
59. Becerra-Carreño, V., Crempien, J. G. F., Benavente, R. & Moreno, M. Plate-locking, uncertainty estimation and spatial correlations revealed with a Bayesian model selection method: application to the central Chile subduction zone. *J. Geophys. Res. Solid Earth* **127**, e2021JB023939 (2022).
60. Moreno, M. S., Bolte, J., Klotz, J. & Melnick, D. Impact of megathrust geometry on inversion of coseismic slip from geodetic data: application to the 1960 Chile earthquake. *Geophys. Res. Lett.* **36**, 16310 (2009).
61. Yu, H., Liu, Y., Yang, H. & Ning, J. Modeling earthquake sequences along the Manila subduction zone: effects of three-dimensional fault geometry. *Tectonophysics* **733**, 73–84 (2018).
62. Condit, C. B., Guevara, V. E., Delph, J. R. & French, M. E. Slab dehydration in warm subduction zones at depths of episodic slip and tremor. *Earth Planet. Sci. Lett.* https://doi.org/10.1016/j.epsl.2020.116601 (2020).
63. Hernández-Uribe, D., Palin, R. M., Cone, K. A. & Cao, W. Petrological implications of seafloor hydrothermal alteration of subducted mid-ocean ridge basalt. *J. Petrol.* **61**, egaa086 (2021).
64. Maldonado, V., Contreras, M. & Melnick, D. A comprehensive database of active and potentially-active continental faults in Chile at 1:25,000 scale. *Sci. Data* **8**, 20 (2021).
65. Melnick, D., Bookhagen, B., Strecker, M. R. & Echtler, H. P. Segmentation of megathrust rupture zones from fore-arc deformation patterns over hundreds to millions of years, Arauco peninsula, Chile. *J. Geophys. Res. Solid Earth* **114**, 1407 (2009).
66. GEBCO Compilation Group *GEBCO 2023 Grid* (National Oceanic Centre & British Oceanographic Data Centre, 2023); https://doi.org/10.5285/836f016a-33be-6ddc-e053-6c86abc0788e
67. NASA EOSDIS Land Processes Distributed Active Archive Center NASA Shuttle Radar Topography Mission Global 1 Arc Second. *NASA JPL* https://doi.org/10.5067/MEaSUREs/SRTM/SRTMGL1.003 (2013).

Methods

Fault friction and mantle viscosity

The stages of the seismic cycle in faults can be described using constitutive relationships of slip-rate- and state-dependent friction that explain the evolution of sliding velocity over time. These laws had been used to model several rupture styles in nature[68] and to characterize the seismic cycle at different tectonic settings. This leads to the possibility of understanding fast and slow ruptures at different fault configurations. Here we use a constitutive framework obtained from the assumption of a microphysical model of the slip-rate- and state-dependent friction under isothermal conditions. In this context, the sliding velocity depends on the density of the real area of contact as follows[69]:

$$V = V_0\left(\frac{\tau}{\mathscr{A}\chi}\right)^{\frac{\mu_0}{a}} \exp\left[-\frac{Q}{R}\left(\frac{1}{T}-\frac{1}{T_0}\right)\right] \tag{1}$$

where V is the sliding velocity, τ is the norm of the shear stress resolved on the fault plane, T is the absolute temperature, μ_0 is the static coefficient of friction at V_0 and T_0, $\mathscr{A}$ is the real area of contact density (real area of contact divided by the nominal surface area), χ is the indentation hardness, $a \ll 1$ is the direct effect, Q is the activation energy and R is the gas constant. The real area of contact depends on the effective normal stress and changes as a function of the shape of the surrounding contact junctions[70]. This last feature is characterized by a state variable that represents the age of the grain, which coincides with the age of contact defined by ref. 71. The relationship between the effective normal stress and the real area of contact is given by[69]:

$$\mathscr{A} = \frac{\mu_0\sigma_{\mathrm{eff}}}{\chi}\left(\frac{\theta V_0}{L}\right)^{\frac{b}{\mu_0}} \tag{2}$$

where σ_{eff} is the effective normal stress, θ is the state variable, L is the characteristic weakening distance associated with the gouge thickness or fault roughness and $b \ll 1$ is the evolution effect. By combining equations (1) and (2), the multiplicative form of slip-rate- and state-dependent friction at isothermal conditions is obtained[24,69]:

$$\tau = \mu_0\bar{\sigma}\left(\frac{V}{V_0}\right)^{\frac{a}{\mu_0}}\left(\frac{\theta V_0}{L}\right)^{\frac{b}{\mu_0}} \tag{3}$$

The state variable under isothermal conditions follows an evolution law which allows healing at the stationary contacts[5,69]:

$$\dot{\theta} = \exp\left[-\frac{H}{R}\left(\frac{1}{T}-\frac{1}{T_0}\right)\right] - \frac{\theta V}{L} \tag{4}$$

Fault dynamics are controlled by the spatial distribution of μ_0, $\bar{\sigma}$, a, b and L, which are governed by the thermal state at the fault interface and by the mineral assembly of the respective stable lithological facie under that state. We assume that those parameters do not change over time and are not affected by heat and fluid transport, which means that the value that controls the frictional behaviour on the fault at steady state will be $a - b$. Depending on its temperature distribution, effective normal stress and rock composition, any given fault can experience a velocity-weakening ($a - b < 0$) or a velocity-strengthening ($a - b > 0$) behaviour[72]. Velocity-weakening areas will experience unstable slip whereas velocity-strengthening regions should slip aseismically[73]. Nonetheless, previous works had shown that velocity-strengthening regions can propagate ruptures[74].

As can be anticipated from equations (3) and (4), there is a very wide spectrum of sliding mechanisms that are generated at the fault over time. This introduces high uncertainties about the distribution of the parameters that govern slip-rate- and state-dependent friction relations. Nevertheless, from a dimensional analysis of the frictional equations, ref. 24 defined two dimensionless parameters that can be understood as two degrees of freedom for the frictional behaviour of a given fault:

$$R_{\mathrm{u}} = \frac{(b-a)\sigma_{\mathrm{eff}}}{G}\frac{W}{L} \tag{5}$$

$$R_b = \frac{b-a}{b} \tag{6}$$

where R_{u} is known as the Dieterich–Ruina–Rice number and depends on the geometry of the fault given by the width W of the velocity-weakening patch, on the frictional behaviour given by $a - b$, on the effective normal stress, and on the shear modulus G at plane strain conditions. For a velocity-weakening segment R_{u} takes positive values and represents the relation between the segment dimension and the nucleation size. Greater values of R_{u} will lead to the nucleation of smaller instabilities with respect to W[24].

The other parameter is R_b, which controls the transient evolutionary effects and the strengthening behaviour. Velocity-strengthening patches will have $R_b < 0$, velocity-weakening domains are characterized by $0 < R_b < 1$ and velocity neutral regimes are defined when $R_b \approx 0$. R_b also controls the rupture propagation in the same way as the ratio a/b[75]. At velocity-weakening domains and high sliding velocities, when a/b is close to the unity, then the rupture will tend to extend towards the whole segment.

The combination of R_{u} and R_b gives a two-dimensional space where different rupture styles can arise. By constraining the spectrum of frictional parameters, the actual slip behaviour of a given fault can be approximated. We use this approach to feed the initial state of all the parameters in our model. We collect a wide range of datasets to constrain the pressure–temperature conditions and the slip mechanism at the plate interface. Then, we assume an initial composition for the oceanic plate and for the sediments at the trench. From that point, we use previous stability fields of subduction related metamorphic facies to define the metamorphic state along dip. Finally, we define the frictional parameters using previous gouge data from different lithologies that represent the metamorphic facies at the plate interface.

The viscoelastic behaviour is calculated using a power-creep law that assumes pure dislocation creep over minerals with a constant water concentration[44]:

$$\dot{\varepsilon} = A\sigma^n C_{\mathrm{OH}}{}^r d^{-m}\exp\left(\frac{-Q+p\Omega}{RT}\right) \tag{7}$$

where $\dot{\varepsilon}$ is the strain rate, A is a pre-exponential factor, σ is the deviatoric stress, C_{OH} is the water concentration, d is grain size, Q is the activation energy, p is the lithostatic pressure, Ω is the activation volume, R is the constant for ideal gasses, T is the temperature and n, r and m are experimentally derived exponents. To yield an expression independent of the grain size, we assume $m = 0$ and $n > 1$ (refs. 44,76).

From this configuration of the subduction fault, we make a meshed subduction system (Extended Data Fig. 1a) to run a numerical model of the subduction seismic cycle. We discretize the system into a triangular mesh of 857 cells with a size of 20 km (Extended Data Fig. 1a), while the points elements at the fault are separated by 200 m along the Slab2 geometry[11], allowing numerical convergence. Deformation at each triangle is computed considering a Burger's assembly where the total anelastic strain rate is given by $\varepsilon_{\mathrm{T}} = \varepsilon_{\mathrm{M}} + \varepsilon_{\mathrm{K}}$, in which ε_{M} and ε_{K} are the instantaneous strain rates in the Kelvin and Maxwell elements, respectively[45]. Power-creep law parameters for the oceanic and continental mantle (Extended Data Table 2) are assumed following previous experimental works and simulations[44,45]. We used the numerical code Unified Cycle of Earthquakes (UniCycIE) that employs the integral method[5,77,78], including surface and volume elements. The changes in fault traction will depend on the surrounding

fault slip and distributed strain. We assume a background strain rate in the horizontal direction of $\varepsilon = -1 \times 10^{-14}$ s^{-1} and predefine a set of synthetic GNSS stations at the surface of our mesh to compare those results with the actual data.

Temperature model

The subduction thermal model is constructed considering an oceanic slab subducting with a kinematically prescribed velocity (66 mm per year)[79] beneath a fixed and layered continental plate. We use the continental lithospheric structure of ref. 19 considering an upper and lower crust, an oceanic crust and a continental and oceanic mantle. In this framework, the downgoing slab drives flow within the overlying viscous mantle wedge.

Velocity and pressure at the mantle wedge are found by solving the equations of mass and momentum conservation. Following ref. 80, we solve the equation of conservation of mass:

$$\nabla \cdot v = 0 \tag{8}$$

and the conservation of momentum:

$$\nabla \cdot \tau - \nabla P = 0 \tag{9}$$

where v is velocity, τ is the deviatoric stress tensor and P is the dynamic pressure. The deviatoric stress tensor is given by:

$$\tau = 2\eta\dot{\varepsilon} \tag{10}$$

in which η is the effective dynamic viscosity and the components of the strain rate tensor ε are:

$$\dot{\varepsilon}_{ij} = \frac{1}{2}\left(\frac{\partial v_i}{\partial x_j} + \frac{\partial v_j}{\partial x_i}\right). \tag{11}$$

We assume that viscosity is obtained by dislocation creep:

$$\eta = A \exp\left(\frac{Q}{nRT}\right)\dot{\varepsilon}^{\frac{(1-n)}{n}}, \tag{12}$$

where the rheological parameters are the same as in equation (7). We consider a temperature- and stress-dependent wet olivine rheology for the mantle wedge[44].

The boundary conditions for mantle wedge are (1) no slip below the rigid overriding plate and (2) constant velocity with a value equal to plate convergence along the top of the slab and below the maximum decoupling depth[81].

The thermal field within the entire subduction zone is computed by solving the steady-state heat advection–diffusion equation, so temperature is obtained by solving:

$$\rho c_p (v \cdot \nabla) T = \nabla \cdot (k \nabla T) + f \tag{13}$$

in which ρ is density, c_p is the specific heat, k is thermal conductivity and f is a parameter that describes possible heat sources.

To solve the system, we assume a constant temperature at the surface of the model (0 °C) and at the bottom of the oceanic lithosphere (1,450 °C). On the slab inflow boundary, we prescribe a geotherm obtained using a half-space cooling model[82] considering an age of 14 million years ago (ref. 83). At the right edge of the model, we assume a conductive geotherm calculated using the thermal properties of Extended Data Table 3, which is then applied along the landward boundary of the overriding plate. Along the inflow part of the wedge, we prescribe a geotherm that is obtained using an adiabatic gradient of 0.4 °C km^{-1} and a mantle potential temperature of 1,300 °C. For the outflow boundary of the wedge, zero heat flux is assumed.

Finally, we solve equations (8), (9) and (11) using a stabilized finite element[41] that allows us to use equal order of polynomial interpolation at each unknown point.

Pressure and temperature path

To compute the pressure–temperature path, we use the lithospheric structure of ref. 19, and we take the average density structure of ref. 84. We compute the vertical stress with:

$$\sigma_v = g\rho h \tag{14}$$

where g is the gravity acceleration constant, ρ is density and h is the thickness of the lithospheric layer (upper crust, lower crust and lithospheric mantle). Then, we compute the normal component over each element of the fault surface to obtain the σ_n. By combining the temperature distribution at the plate interface and the σ_v over it, we obtain the pressure–temperature path from Extended Data Fig. 1b.

Coseismic slip model

We invert the coseismic slip for the dip direction using the uplift displacements on the surface from the work of ref. 8 in between 42° S and 45° S.

To find the solution, we apply the Bayesian inversion approach of ref. 59, which allows us to obtain positive model parameters and associated uncertainties. This constraint allows us to obtain a more realistic slip solution as the slip direction is positive with respect to the dip direction, given the subduction stress regime. We impose a slip solution to be a multivariate folded normal distribution, and simultaneously we seek to find a solution for $Gm = d$, where d is the deformation data, m is the backslip on each subfault in the plate contact and G is the matrix which contains the Green's functions. The Bayesian formulation is given by:

$$p(s|d,H) = \frac{p(d|s)p(s \vee H)}{p(d \vee H)} \tag{15}$$

with

$$p(s \vee H) = (2\pi)^{\frac{-N_m}{2}} |S|^{\frac{-1}{2}} \exp\left[\frac{1}{2}(s^p - s)^T S^{-1}(s^p - s)\right] \tag{16}$$

$$p(d \vee s) = (2\pi)^{\frac{-N_d}{2}} |D|^{\frac{-1}{2}} \exp\left[\frac{-1}{2}(d - G|s|)^T D^{-1}(d - G|s|)\right] \tag{17}$$

To enforce positivity constraints on the model parameters, we impose the following changes of variables:

$$m(s) = (|s_1|, |s_2| \ldots, |s_m|)^T \tag{18}$$

which guarantees us a positive solution and results in a folded normal distribution in the posterior distribution.

We use the maximum evidence criteria to perform Bayesian model selection, namely, to search for the hyperparameters of a particular hypothesis H. D and S are the covariance matrices of the likelihood and prior, respectively. The mean of the prior is s^p. We then obtain the correlation between the slip parameters based on the information of the same data.

Data availability

The GPS data that support the findings of this study are available in the GNSS data repository of the Centro Sismologico Nacional, Chile (http://gps.csn.uchile.cl/data/). Uplift data after the Valdivia earthquake can be found at ref. 8 (https://doi.org/10.1130/0016-7606(1970)81[1001:MOTCEO]2.0.CO;2). Data of intertidal biotic indicators were obtained from ref. 50 (https://doi.org/10.1130/0016-7606(1970)81[1001:MOTCEO]2.0.CO;2). Thermal model, coseismic slip model and quasi-dynamic input

files to be run using Unicycle are uploaded to https://doi.org/10.5281/zenodo.8435744. Specific results from the quasi-dynamic simulations are available from the corresponding author upon reasonable request.

Code availability

Quasi-dynamic simulations were computed using the code Unicycle[5,85] (https://bitbucket.org/sbarbot/unicycle/src/master/). The code to process quasi-dynamic results is available from the corresponding author upon reasonable request.

References

68. Lapusta, N. & Rice, J. R. Nucleation and early seismic propagation of small and large events in a crustal earthquake model. *J. Geophys. Res. Solid Earth* **108**, 2205 (2003).
69. Barbot, S. Modulation of fault strength during the seismic cycle by grain-size evolution around contact junctions. *Tectonophysics* **765**, 129–145 (2019).
70. Dieterich, J. H. & Kilgore, B. Implications of fault constitutive properties for earthquake prediction. *Proc. Natl Acad. Sci. USA* **93**, 3787–3794 (1996).
71. Dieterich, J. H. Modeling of rock friction 1. experimental results and constitutive equations. *J. Geophys. Res. Solid Earth* **84**, 2161–2168 (1979).
72. Marone, C. Laboratory-derived friction laws and their application to seismic faulting. *Annu Rev. Earth Planet Sci.* **26**, 643–696 (1998).
73. Bürgmann, R. The geophysics, geology and mechanics of slow fault slip. *Earth Planet. Sci. Lett.* **495**, 112–134 (2018).
74. Kozdon, J. E. & Dunham, E. M. Rupture to the trench: dynamic rupture simulations of the 11 March 2011 Tohoku earthquake. *Bull. Seismol. Soc. Am.* **103**, 1275–1289 (2013).
75. Rubin, A. M. & Ampuero, J. P. Earthquake nucleation on (aging) rate and state faults. *J. Geophys. Res. Solid Earth* **110**, 1–24 (2005).
76. Hirth, G. & Kohlstedt, D. Rheology of the upper mantle and the mantle wedge: a view from the experimentalists. *Geophys. Monogr. Ser.* **138**, 83–105 (2004).
77. Barbot, S., Moore, J. D. P. & Lambert, V. Displacement and stress associated with distributed anelastic deformation in a half-space. *Bull. Seismol. Soc. Am.* **107**, 821–855 (2017).
78. Muto, J. et al. Coupled afterslip and transient mantle flow after the 2011 Tohoku earthquake. *Sci. Adv.* **5**, eaaw1164 (2019).
79. Marotta, G. S. A., França, G. S., Galera Monico, J. F., Fuck, R. A. & Oswaldo de Araújo Filho, J. Strain rate of the South American lithospheric plate by SIRGAS-CON geodetic observations. *J. South Am. Earth Sci.* **47**, 136–141 (2013).
80. van Keken, P. E. et al. A community benchmark for subduction zone modeling. *Phys. Earth Planet. Inter.* **171**, 187–197 (2008).
81. Peacock, S. M. & Wang, K. On the stability of talc in subduction zones: a possible control on the maximum depth of decoupling between the subducting plate and mantle wedge. *Geophys. Res. Lett.* **48**, e2021GL094889 (2021).
82. Turcotte, D. & Schubert, G. *Geodynamics* (Cambridge Univ. Press, 2014); https://doi.org/10.1017/CBO9780511843877
83. Tebbens, S. F. & Cande, S. C. Southeast pacific tectonic evolution from early oligocene to present. *J. Geophys. Res. Solid Earth* **102**, 12061–12084 (1997).
84. Tassara, A. Control of forearc density structure on megathrust shear strength along the Chilean subduction zone. *Tectonophysics* **495**, 34–47 (2010).
85. Barbot, S. Asthenosphere flow modulated by megathrust earthquake cycles. *Geophys. Res. Lett.* **45**, 6018–6031 (2018).
86. Phillips, N. J., Belzer, B., French, M. E., Rowe, C. D. & Ujiie, K. Frictional strengths of subduction thrust rocks in the region of shallow slow earthquakes. *J. Geophys. Res. Solid Earth* **125**, e2019JB018888 (2020).

Acknowledgements

This work is supported by the National Agency of Research and Development (ANID-Human Resources Branch/National Doctorate/2021) (J.J.), the Millennium Scientific Initiative (ICM) grant NC160025 'CYCLO—the seismic cycle along subduction zones' (A.T., J.J.). R.A. acknowledges funding from the Centro de Modelamiento Matemático (FB210005) of the PIA Program: Concurso Apoyo a Centros Científicos y Tecnológicos de Excelencia con Financiamiento Basal (ANID-Chile). S.B. acknowledges funding from the National Science Foundation under award number EAR-1848192. J.G.F.C. has been supported by Centro de Investigación para la Gestión Integrada del Riesgo de Desastres (CIGIDEN), Agencia Nacional de Investigación y Desarrollo (ANID)/Fondo de Financiamiento de Centros de Investigación en Áreas Prioritarias (FONDAP)/1522ª0005 and acknowledges support from ANID/Fondo Nacional de Desarrollo Científico y Tecnológico (FONDECYT)/11201180. M.M. acknowledges support from ICN12019N Instituto Milenio de Oceanografía and FONDECYT 1221507 and CIGIDEN (FONDAP)/1522ª0005.

Author contributions

J.J., S.B., M.M. and A.T. conceived the original idea, which was elaborated with J.G.F.C. and R.A. Quasi-dynamic numerical simulations were performed by J.J. using the numerical code of S.B. N.C. and R.A. made the thermal model, V.B-C. and J.G.F.C. computed the coseismic slip model. J.J. compiled the geophysical and structural data to then build the representative cross section. J.J. estimated the pressure–temperature path along plate interface. The paper was written by J.J. and S.B. with comments of M.M., A.T., J.G.F.C. and R.A.

Competing interests

The authors declare no competing interests.

Additional information

Extended data is available for this paper at https://doi.org/10.1038/s41561-023-01327-8.

Supplementary information The online version contains supplementary material available at https://doi.org/10.1038/s41561-023-01327-8.

Correspondence and requests for materials should be addressed to Joaquín Julve.

Peer review information *Nature Geoscience* thanks Mohamed Chlieh, Muriel Gerbault and the other, anonymous, reviewer(s) for their contribution to the peer review of this work. Primary Handling Editors: Stefan Lachowycz and Alison Hunt, in collaboration with the *Nature Geoscience* team.

https://doi.org/10.1038/s41561-023-01327-8

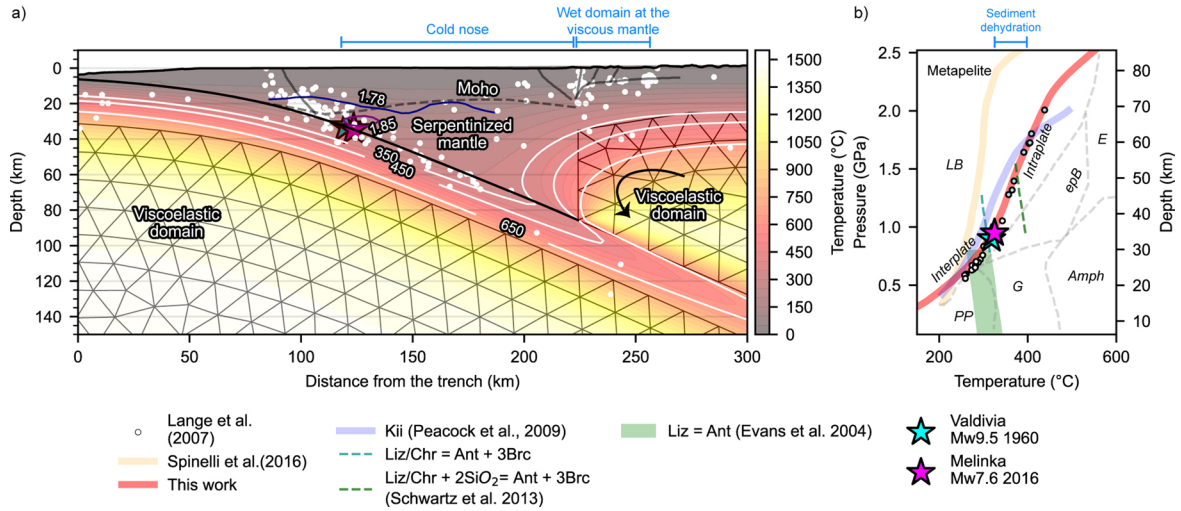

Extended Data Fig. 1 | Temperature distribution, mesh, and pressure-temperature path. a) black arrow denotes the convective asthenosphere flux. Purple curves are contours of the Vp/Vs value[21]. Triangles are the mesh used for the continental and oceanic mantle. **b**) Gray dashed lines are the limits of metamorphic facies for a metapelite rock[62]. LB = Lawsonite Blueschist, epB = Epidote Blueschist, Amph = Amphibolite, G = Greenschist, PP = Prehnite-Pumpellyite, E = Eclogite. Intraplate and Interplate refer to the location of the interseismic seismicity.

https://doi.org/10.1038/s41561-023-01327-8

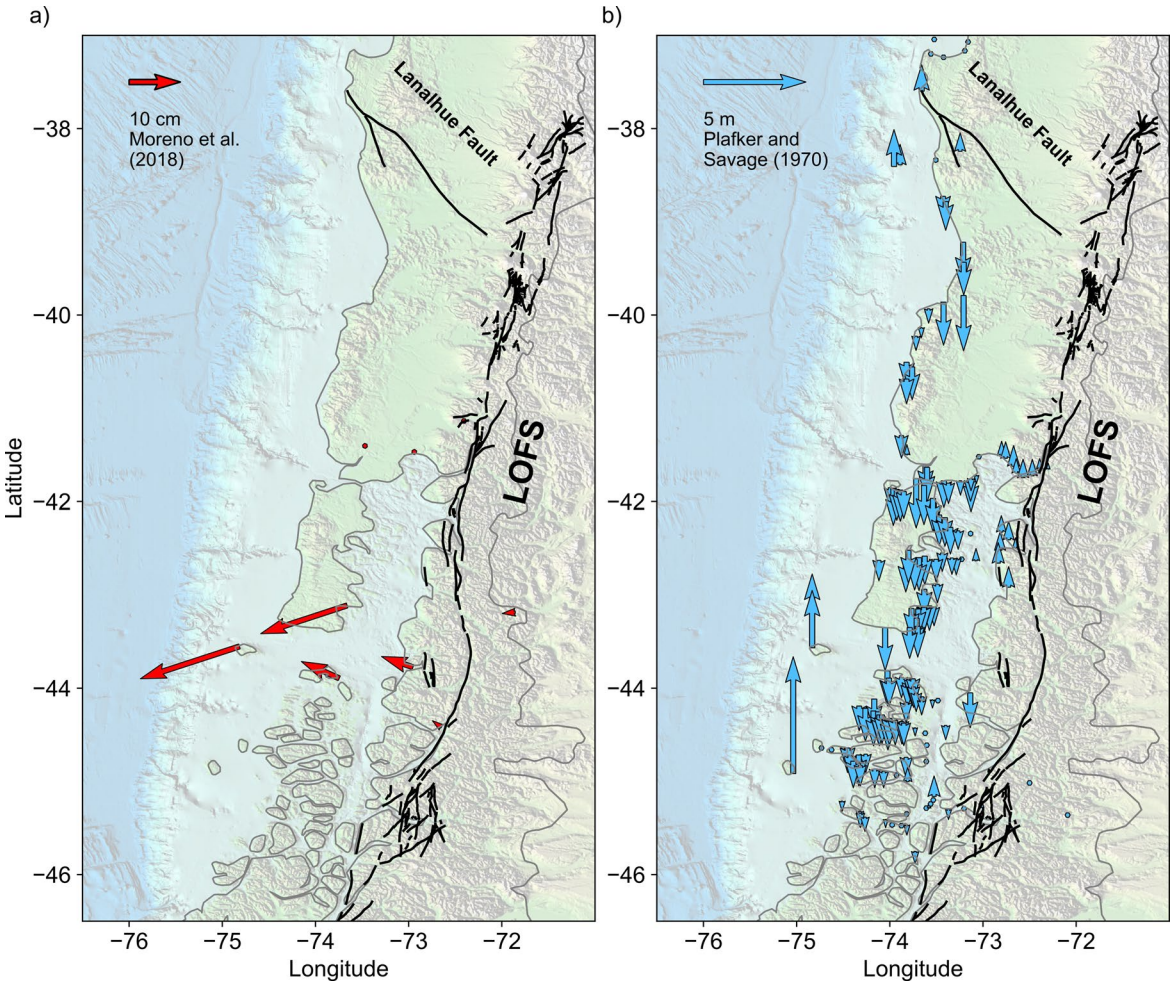

Extended Data Fig. 2 | GNSS and intertidal biotic indicator data. a) Velocity vectors from ref. 40 for the coseismic slip of the Melinka Mw7.6 2016 earthquake. **b**) Uplift data from ref. 8 measured after 8 years of the Valdivia Mw9.5 1960 earthquake. Basemap from GEBCO.

https://doi.org/10.1038/s41561-023-01327-8

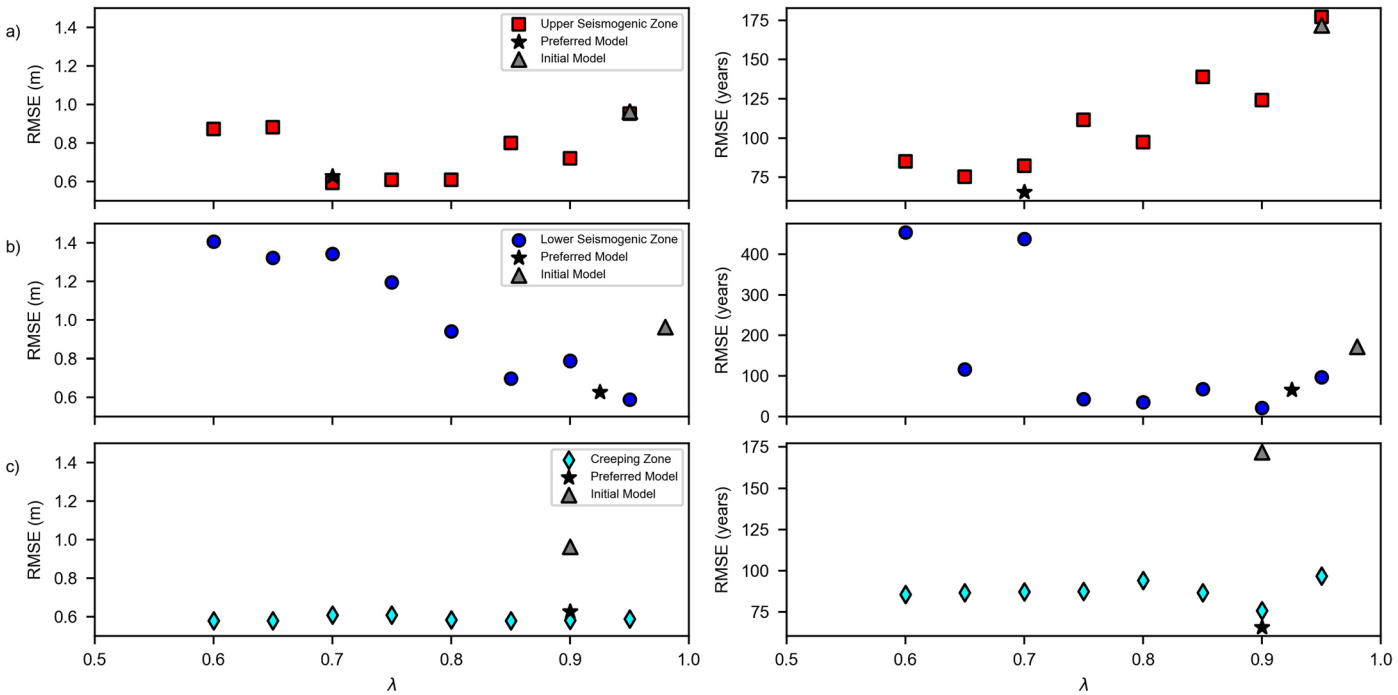

Extended Data Fig. 3 | Root mean squared error values for systematic variation on λ. In the left column are plotted RMSE values with respect to the surface deformation obtained from GNSS data of Melinka and Valdivia earthquakes. In the right column are plotted RMSE values with respect to the median value of great and large earthquakes obtained from the paleoseismic record. Red squares are the models in which the λ value is changed in the Upper Seismogenic Zone. Blue dots are the models in which the λ value is changed in the Lower Seismogenic Zone. Creeping zone in c) refers to the Metamorphic Belt and Serpentinized Mantle Wedge segments. Light blue diamonds are the models in which the λ value is changed in the Creeping Zone domain.

https://doi.org/10.1038/s41561-023-01327-8

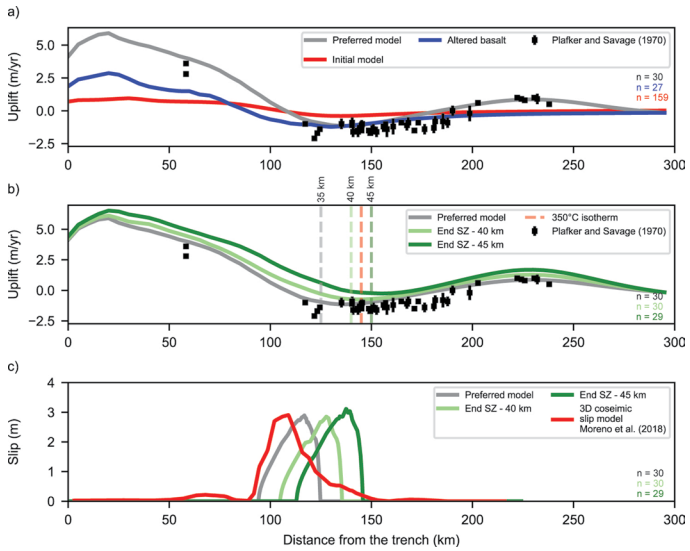

Extended Data Fig. 4 | Effects of petrology and depth of the end of the seismogenic zone. In a) the gray curve is the median coseismic slip for great ruptures from the preferred model. The blue curve is the median coseismic slip for great ruptures from a model in which the Upper and Lower Seismogenic Zone are controlled by the frictional behavior of altered basalt ($a-b$ and μ_o are obtained from ref. 86 while the rest of frictional parameters are the same as the preferred model in Table 1). The red curve is the median coseismic slip for great ruptures from the initial model. In b) gray and green curves show the median coseismic slip for great ruptures in which the end of the seismogenic zone is increased. Isotherm in b) is obtained from our computed thermal distribution. Gray and green dashed curves mark the depth in which ends the seismogenic zone for each model. Error bars in data of Plafker and Savage are reported as mean errors as function of the methodology in which uplift was measured. In c) the red curve is the interpolation at 43° S of the 3D coseismic slip model from ref. 40. Gray and green curves are the mean coseismic slip distribution for large ruptures, with the same changes in the end of the seismogenic zone as b).

https://doi.org/10.1038/s41561-023-01327-8

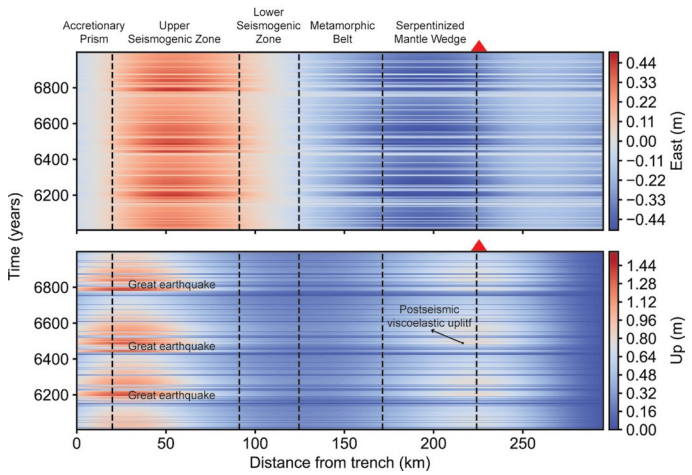

Extended Data Fig. 5 | Time series of the east and vertical components of the synthetic gps from our model. We select the same time interval from Fig. 3. Red triangles mark the position of the volcanic arc.

https://doi.org/10.1038/s41561-023-01327-8

Extended Data Table 1 | Power-creep law properties

Volume	A ($MPa^{-n}s^{-1}$(ppm H/Si)$^{-r}$)	r	C_{OH} (ppm H/Si)-	n	Ω (cm^3/mol)	Q (Kj/mol)
Oceanic Mantle	$10^{0.56}$	1.2	1000	3	1.30E-05	5.10E+05
Continental Mantle (dry conditions)	$10^{0.56}$	1.2	1000	3	1.10E-05	4.75E+05
Continental Mantle (wet conditions below the arc)	$10^{0.56}$	1.2	1200	3	1.10E-05	5.10E+05

Initial values were obtained from refs. 44,76.

https://doi.org/10.1038/s41561-023-01327-8

Extended Data Table 2 | Pore pressure ratio and effective normal stress variation

USZ		LSZ		CZ			
				MB		AB	
λ	σ (Mpa)	λ	σ (Mpa)	λ	σ (Mpa)	λ	σ (Mpa)
0.6	150	0.6	300	0.6	520	0.6	880
0.65	131	0.65	263	0.65	455	0.65	770
0.7	113	0.7	225	0.7	390	0.7	660
0.75	94	0.75	188	0.75	325	0.75	550
0.8	75	0.8	150	0.8	260	0.8	440
0.85	56	0.85	113	0.85	195	0.85	330
0.9	38	0.9	75	0.9	130	0.9	220
0.95	19	0.95	38	0.95	65	0.95	110

USZ = Upper seismogenic zone, LSZ = Lower Seismogenic Zone, MB = Metamorphic Belt, AB = Ancud Basin, CZ = Creeping Zone.

https://doi.org/10.1038/s41561-023-01327-8

Extended Data Table 3 | Thermal properties of the temperature model

Layer	Thermal conductivity (W/mK)	Radiogenic heat production ($\mu W/m^3$)	Density(kg/m^3)	Specific heat (J/kgK)
Upper continental Crust	2.9	1.3	2700	1000
Lower Continental Crust	2.9	0.4	3300	1000
Oceanic Crust	3.1	0.02	3300	1000
Oceanic and Continental Mantle	3.1	0.02	3300	1000